Resolving dynamic fragmentation of liquids at the nanoscale with ultrafast small-angle X-ray scattering

6 authors, including:

Sen Chen
The Peac Institute of Multiscale Sciences
27 PUBLICATIONS   97 CITATIONS

SEE PROFILE

Haiwei Chai
The Peac Institute of Multiscale Sciences
13 PUBLICATIONS   114 CITATIONS

SEE PROFILE

An-Min He
Institute of Applied Physics and Computational Mathematics
91 PUBLICATIONS   672 CITATIONS

SEE PROFILE

Yang Cai
The Peac Institute of Multiscale Sciences
49 PUBLICATIONS   381 CITATIONS

SEE PROFILE

Some of the authors of this publication are also working on these related projects:

Project   Dynamic SAXS Experiments on Synchcrotrons and XFELs View project

Project   crystallization View project

Resolving dynamic fragmentation of liquids at the nanoscale with ultrafast small-angle X-ray scattering

Sen Chen,[a,b] **Hai-Wei Chai,**[a,b] **An-Min He,**[c] **Thomas Tschentscher,**[d] **Yang Cai**[a]* **and Sheng-Nian Luo**[a,b]*

[a]The PEAC Institute of Multiscale Sciences, Chengdu, Sichuan 610031, People's Republic of China, [b]Key Laboratory of Advanced Technologies of Materials, Ministry of Education, Southwest Jiaotong University, Chengdu, Sichuan 610031, People's Republic of China, [c]Institute of Applied Physics and Computational Mathematics, Beijing 100094, People's Republic of China, and [d]European XFEL GmbH, Schenefeld, Germany. *Correspondence e-mail: caiy@pims.ac.cn, sluo@pims.ac.cn
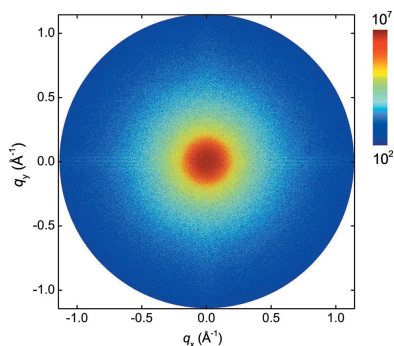
High-brightness coherent ultrashort X-ray free-electron lasers (XFELs) are promising in resolving nanoscale structures at the highest temporal resolution (~10 fs). The feasibility is explored of resolving ultrafast fragmentation of liquids at the nanoscale with single-shot small-angle X-ray scattering (SAXS) on the basis of large-scale molecular dynamics simulations. Fragmentation of liquid sheets under adiabatic expansion is investigated. From the simulated SAXS patterns, particle-volume size distributions are obtained with the regularization method and average particle sizes with the weighted Guinier method, at different expansion rates. The particle sizes obtained from simulated SAXS are in excellent agreement with direct cluster analysis. Pulse-width effects on SAXS measurements are examined. The results demonstrate the feasibility of resolving the nanoscale dynamics of fragmentation and similar processes with SAXS, and provide guidance for future XFEL experiments and data interpretation.

1. Introduction

Dynamic fragmentation is ubiquitous in nature and engineering (Grady, 2007, 2010; Boast & Baveye, 2017) and the physics governing these processes varies considerably (Michel *et al.*, 2001; Holian & Grady, 1988; Grady, 2009; Åström *et al.*, 2000; Sorenson *et al.*, 2017; Durand & Soulard, 2013). For such highly transient, irreversible and nonlinear fragmentation processes, establishing reliable predictive capabilities is of great interest. For example, fragment-size or mass-distribution evolution is a key question to be answered for dynamic fracture and failure (Grady, 2010). Various strategies have been proposed for *in situ* real-time measurements on different length scales, such as optical and X-ray phase-contrast imaging (Monfared *et al.*, 2014), proton radiography (Buttler *et al.*, 2012; Morris *et al.*, 2016), holography (Sorenson *et al.*, 2017) and Mie scattering (Monfared *et al.*, 2015).

Nanoscale dynamic fragmentation, however, is inaccessible by the techniques mentioned above due to their limited spatial resolution (Sorenson *et al.*, 2017; Monfared *et al.*, 2015), and measuring particle-size distribution at the nanoscale has been a challenge for dynamic events such as inertial-confinement fusion (Sorenson *et al.*, 2014; Goncharov, 1999; Thomas & Kares, 2012). Molecular dynamics (MD) simulations are currently the main means of investigating nanoscale fragmentation. A large number of MD simulations have investigated dynamic jetting and fragmentation, addressing the effects of strain rate (Holian & Grady, 1988; Wagner *et al.*, 1992; Ashurst & Holian, 1999), surface roughness and load

intensity (Durand & Soulard, 2013, 2012; He *et al.*, 2016), and defect morphology (Li, Zhao *et al.*, 2014; Li, Wang *et al.*, 2014). However, direct measurements of dynamic fragmentation are still lacking and very desirable.

Due to the highly transient nature of dynamic fragmentation, measurements at the nanoscale must be single-shot with high spatial and temporal resolution. Small-angle X-ray scattering (SAXS) can provide information on the size, shape and size distributions of nanoparticles. The very bright coherent ultra-short pulses from X-ray free-electron lasers (XFELs) offer promise in resolving nanoscale structures at the highest temporal resolution ($\sim$10 fs), while SAXS measurements with synchrotron sources may suffer a lower signal-to-noise ratio due to the limited number of photons within a single pulse, and a lower temporal resolution due to their longer pulse duration ($\sim$100 ps) in the case of dynamic measurements. An open question is whether nanoscale fragmentation dynamics can be resolved with ultrafast SAXS.

In this work, we utilize large-scale MD simulations and single-shot SAXS simulations to explore the feasibility of resolving nanoscale fragmentation of liquids with XFEL SAXS, to guide future experiments and data interpretation. Large-scale MD simulations are used to simulate the adiabatic expansion of liquid microsheets at different expansion rates. SAXS patterns are obtained from atomic configurations at different stages of fragmentation. From the simulated SAXS patterns, we obtain particle-volume size distributions with the regularization method and average particle sizes with the weighted Guinier method. The particle sizes as obtained from simulated SAXS are compared with those obtained from direct cluster analysis of MD configurations. Anisotropic 2D SAXS patterns at early stages of fragmentation are also investigated. The effect of X-ray pulse width on the potential SAXS measurements is examined. Our results demonstrate the feasibility of the proposed SAXS measurements.

2. Methodology

2.1. Molecular dynamics simulations and cluster analysis

An accurate embedded-atom model (EAM) potential for Cu (Mishin *et al.*, 2001) is used to describe its thermo-mechanical properties under both equilibrium and non-equilibrium loading conditions (An *et al.*, 2008; Bringa *et al.*, 2004; Li *et al.*, 2010), including surface tension and viscosity (Cai *et al.*, 2014). MD simulations are performed with the large-scale atomic/molecular massively parallel simulator (*LAMMPS*) (Plimpton, 1995).

We first construct a single-crystal Cu sheet consisting of 38.4 million atoms, or $2000 \times 150 \times 8$ elementary cells along the x, y and z axes, respectively. Crystallographic orientations $\langle 100 \rangle$, $\langle 010 \rangle$ and $\langle 001 \rangle$ are along the x-, y- and z-axes. (The coordinate system is defined in Fig. 1.) The initial liquid Cu configuration is obtained by melting the single-crystal configuration at zero pressure and 2000 K with the constant pressure–temperature ensemble, and equilibrated at 1400 K; the dimensions of the resultant liquid sheet are

$1511.1 \times 113.3 \times 3.0$ nm. Then, a linear velocity gradient along the x axis is imposed within the sheet for a given expansion rate (η), while the velocity gradients are set to zero (except for thermal fluctuations) along the y and z axes.

Simulations of the fragmentation of adiabatically expanding liquid sheets are performed with the microcanonical ensemble, and the periodic boundary condition is applied only along the y axis. The equation of motion is integrated via the Verlet algorithm with a time step of 1 fs, and the run durations are up to 500 ps to achieve full fragmentation. The atomic configurations at full fragmentation are analyzed via cluster analysis to obtain particle-size distributions. Four η values, 0.075, 0.1, 0.125 and 0.15 ps^{-1}, are explored to investigate the effect of rate on fragmentation.

To analyze particle shapes at full fragmentation, the surface area and volume for each particle are obtained. An algorithm based on the alpha complex concept (Edelsbrunner & Mücke, 1994) is used to generate a Delaunay tessellation of the atomic configuration (Stukowski, 2014). The triangulated surface is constructed via a dividing surface between occupied (particle interior) and empty regions, which consists of all triangular facets of the Delaunay tessellation. The total surface area of each particle is obtained by summing all triangular facets, and similarly for the total volume of the solid regions.

To elucidate the statistical features of the particle-size distributions in log–log or linear plots, two kinds of size-distribution functions are considered here. One is the particle-number size distribution in terms of particle volume, $\Psi(V)$, which is the particle-number density of a statistical bin centered at V with a bin width of ΔV. ΔV is set to increase with increasing V, following a power law with an exponent of 1.5. In this way, the particle number is statistically significant for sparsely populated large particles (Bontaz-Carion & Pellegrini, 2006). In practice, the particle-number distribution is represented by (V_i, Ψ_i) pairs for $i \geq 1$, with $V_i = (1.5^{i-1} \times 1.5^i)^{1/2} V_0$ and the corresponding number density

$$\Psi_i = \frac{n_i}{(1.5^i - 1.5^{i-1})V_0}. \tag{1}$$

Here, n_i is the number of particles with a volume V satisfying $1.5^{i-1} V_0 \leq V < 1.5^i V_0$, and V_0 is the smallest particle volume preset in the particle-size or cluster analysis. $\Psi(V)$ is used in a
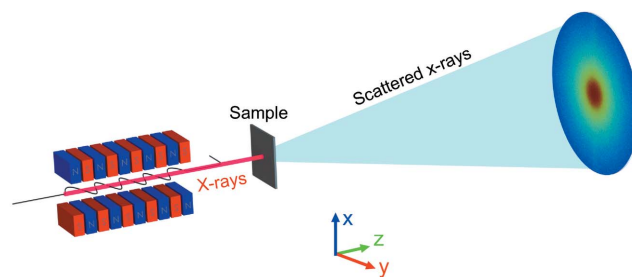
Figure 1
A schematic diagram of the setup for the simulated SAXS measurements on liquid fragmentation with an XFEL. The detector is 240 mm from the sample (a liquid sheet in our case). The incident X-ray beam is perpendicular to the liquid sheet sample.

log–log plot. Another distribution is the particle-volume size distribution, $S(R)$, usually used in SAXS analysis,

$$S(R) = \Psi(R) V(R). \tag{2}$$

Here, $\Psi(R)$ is the number size distribution in terms of R, which can be obtained from $\Psi(V)$. The bin width ΔR is fixed for $\Psi(R)$ and $S(R)$. $S(R)$ is used in linear plots.

2.2. Small-angle X-ray scattering simulations

For the intended experiments on liquid fragmentation, SAXS measurements are necessarily single-shot and single-pulse, and can be photon-starved due to the highly transient nature of dynamic fragmentation, such as in the breaking of ejecta from a perturbed surface under intense shock loading. A typical pulse length of an XFEL is 10 fs, so motion blur can be neglected. To obtain higher photon flux, a pink-beam XFEL with a full undulator bandwidth (up to 1%) may be used for such SAXS measurements, and the impact of 1% bandwidth on data interpretation can be neglected for both polydisperse and monodisperse systems (Chen & Luo, 2018).

To simulate XFEL SAXS patterns of nanoscale liquid fragments, the kinematic approximation is used, which assumes full coherence of incident X-rays and single elastic scattering. A uniform beam-intensity distribution is applied in simulations. Snapshots of a large number of nanoparticles from MD simulations are used as the input atomic positions for SAXS calculations with the GPU accelerated atom-based polychromatic scattering and diffraction simulation code, *GAPD*, developed by the PIMS X-ray Group (E *et al.*, 2018). *GAPD* can deal with atomic systems with arbitrary particle concentrations, dispersities and shapes, ultra-large system sizes (*e.g.* 10 billion atoms), and polychromatic X-rays. The total scattering intensity I of M atoms in a system is computed as the product of the structure factor $F(\mathbf{q})$ with its complex conjugate, $F^*(\mathbf{q})$ (Warren, 1969),

$$I(\mathbf{q}) = F^*(\mathbf{q}) F(\mathbf{q}), \tag{3}$$

with

$$F(\mathbf{q}) = \sum_{j=1}^{M} f_j \exp(i\mathbf{q} \cdot \mathbf{r}_j). \tag{4}$$

Here, $\mathbf{r}_j$ is the position of atom j in real space, f_j is the atomic scattering factor (Fox *et al.*, 1989) and $\mathbf{q}$ is the scattering vector in reciprocal space,

$$\mathbf{q} = \frac{2\pi}{\lambda}(\mathbf{s} - \mathbf{s}_0) = \mathbf{k} - \mathbf{k}_0, \tag{5}$$

where $\mathbf{s}$ and $\mathbf{s}_0$ are unit vectors representing the scattered and incident beam directions, and $\mathbf{k}$ and $\mathbf{k}_0$ are the scattered and incident wavevectors, respectively.

The full coherence of XFELs leads to interparticle interference and the beam-size effect in practical SAXS measurements, which are not adequately considered in traditional SAXS simulations. These two factors may have a strong impact on scattering patterns at small angles and are considered here. In the calculation, the normally used 3D grid in reciprocal space is replaced with 'spherical sampling'. We divide a circle on the Ewald sphere at a given scattering angle 2θ into fine segments at an angle increment of $d\varphi = \text{constant} \times (\sin 2\theta)^{\alpha}$. The constant and the exponent α determine the number of $\mathbf{q}$ points on the circle and modulate $d\varphi$ as desired. $\alpha = \frac{1}{2}$ is used in this study. Different circles represent different 2θ with an equal interval $d(2\theta)$.

Having calculated intensities for all reciprocal points, we then project these reciprocal points onto a position-sensitive detector in real space. The detector is positioned perpendicular to the incident direction of the X-rays and the direct beam points to the center of the detector.

For ultrafast liquid jets (*e.g.* 10 km s^{-1}), a main concern is whether the X-ray pulse width leads to 'motion blur' in SAXS measurements. The scattering intensity $\tilde{I}$ at a given $\mathbf{q}$ in reciprocal space with a finite pulse length τ can be calculated via (Kluge *et al.*, 2014)

$$\tilde{I}(\mathbf{q}) = \frac{1}{\tau} \int_{t}^{t+\tau} I(\mathbf{q}, t)\, \mathrm{d}t. \tag{6}$$

For XFELs, the pulse intensity fluctuates between different pulses and varies with time. For simplicity, we assume the intensity of the incident X-rays to be independent of time and the total number of photons to be fixed for different pulse widths. The results in this work are not affected by this approximation.

In this work, the X-ray wavelength is set at 1.5 Å [corresponding to an XFEL at the Linac Coherent Light Source (LCLS) or the European XFEL], although pink-beam SAXS patterns can be calculated as well (Chen & Luo, 2018). The beam sizes are set to be the same as the system sizes in the MD simulations. The incident direction of the X-rays is set to be along the plane normal of a liquid sheet (the z axis). The parameters of the AGIPD detector of the European XFEL are used and the detected q range is 0–1.3 Å^{-1}. The schematic setup for the simulated SAXS measurements is shown in Fig. 1.

3. Adiabatic expansion and fragmentation of a liquid sheet

MD simulations of the adiabatic expansion of liquid sheets are performed at different expansion rates. The system widths in the y direction are fixed at 1.5 µm, and the lengths of the systems in the x-direction with different expansion rates range from 4 to 6 µm. Adiabatic expansion of a liquid sheet with a velocity gradient of $\eta = 0.1$ ps^{-1} is used as an example to illustrate the fragmentation process, underlying mechanisms and data-analysis methodology.

3.1. The three stages of fragmentation of a liquid sheet

Fig. 2 shows the evolution of the atomic configurations of a liquid sheet during adiabatic expansion (0–440 ps), which can be divided approximately into three stages: the formation of a 2D cellular structure via void nucleation and growth (0–60 ps); disintegration of cells (100 ps); and full fragmentation
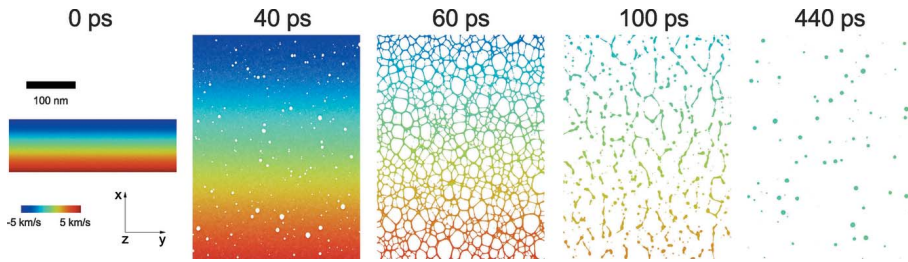
Figure 2
Snapshots of fragmentation showing three stages during uniaxial adiabatic expansion of a liquid microsheet at $\eta = 0.1$ ps^{-1}: the formation of a 2D cellular structure via void nucleation and growth (0–60 ps); disintegration of the closed-cell structure (100 ps); and full fragmentation (440 ps).

$$\Phi_{w,i} = \frac{\sum_{1.5^{i-1}V_0 \leq V_p < 1.5^i V_0} \Phi V_p^2}{\sum_{1.5^{i-1}V_0 \leq V_p < 1.5^i V_0} V_p^2}. \qquad (8)$$

The volume-squared-weighted mean sphericity of particles at full fragmentation is shown in Fig. 3 as a function of particle size, along with the corresponding upper and lower limits within a statistical bin. The fluctuations on the lower-limit curve are due to the fact that particles are at different stages of development towards the perfect s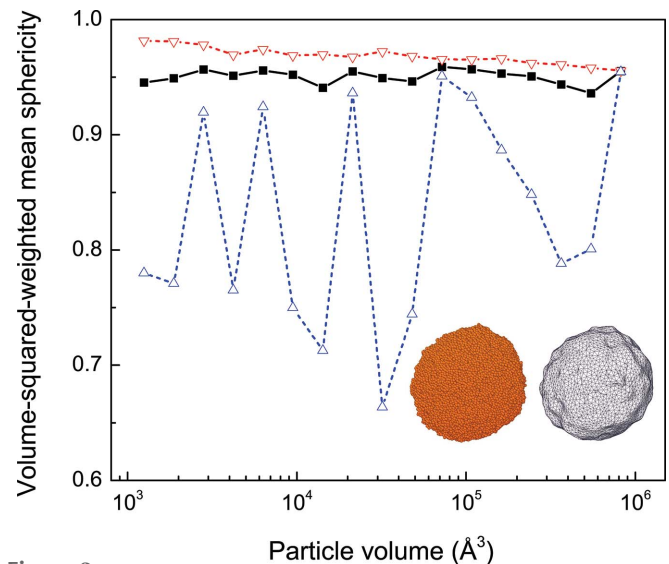pherical shape. The average sphericity is 0.95 ± 0.01 and the Φ_w curve is much closer to the upper-limit curve, indicating that most particles are predominantly spherical. In the following discussions, particles at full fragmentation are assumed to be perfect spheres.

The particle-number size distribution Ψ in terms of particle volume V is derived, and can be well described with the combination of a power law and an exponential law (Fig. 4),

$$\Psi(V) = A_p V^{-1.15} + A_e \exp\left(-\frac{V}{V_c}\right), \qquad (9)$$

where A_p and A_e are constants, and V_c denotes the characteristic particle size. This is in good agreement with previous results obtained by shock-induced jetting from a groove (Durand & Soulard, 2013) and from adiabatic expansion of a liquid sheet at a much slower rate (He *et al.*, 2015). For example, the same exponent (1.15) is obtained from our fit and by Durand & Soulard (2012) for the power law.

The power law in equation (9) describes small sizes and originates from the breakup of 2D cells (stage 2), and an analogy between this process and the 2D percolation process

(440 ps). Similar phenomena have been observed in both MD simulations and experiments (Durand & Soulard, 2012, 2013; Sorenson *et al.*, 2014, 2017; He *et al.*, 2015).

3.1.1. Stage 1: the formation of a 2D cellular structure. The preset velocity gradient leads to in-plane tension and random void nucleation via thermal fluctuations (cavitation; 0–100 ps). Void growth and coalescence result in the formation of a 2D cellular structure consisting of interconnecting 1D cell walls (100–200 ps).

3.1.2. Stage 2: disintegration of cells. The cell walls undergo further tension and the cells begin to disintegrate, producing small particles and long filaments. The small particles achieve stress equilibrium and form spheres; this process can be attributed to 2D percolation theory (Durand & Soulard, 2013; He *et al.*, 2015).

3.1.3. Stage 3: full fragmentation. To achieve stress equilibrium, the 1D filaments break via the Poisson fragmentation process into smaller pieces which become spherical particles of different sizes, and the system become statistically stabilized (440 ps; full fragmentation). The spherical shape is due to the effect of surface tension. The surface energy is added via partial conversion of the kinetic energy (energy balancing). The leading edges of the liquid sheets also fragment via the Poisson process, but are excluded in the discussion below.

3.2. Particle-shape and -size distribution analysis

Particle shapes at full fragmentation are characterized with sphericity. The 3D sphericity Φ of a given particle with a volume V_p and surface area S_p is defined as (Wadell, 1935)

$$\Phi = \frac{\pi^{1/3}(6V_p)^{2/3}}{S_p}. \qquad (7)$$

$\Phi < 1$ for non-spherical particles and $\Phi = 1$ for ideal spherical particles. The surface area and volume for each particle at full fragmentation are obtained by Delaunay tessellation of the whole atomistic configuration. The inset of Fig. 3 presents a typical particle configuration (left) at full fragmentation and (right) the corresponding reconstructed surface mesh. Since SAXS signals are volume-squared sensitive, we define the volume-squared-weighted mean sphericity Φ_w. Binning of particle sizes, similar to the particle-number size-distribution calculation, is also used. Φ_w for the ith bin is obtained via

Figure 3
Volume-squared-weighted mean sphericity (Φ_w) for particles of different sizes at full fragmentation ($\eta = 0.1$ ps^{-1}) (black solid symbols and line). Red and blue open symbols/dashed lines denote the maximum and minimum sphericities within a given bin, respectively. Inset: (left) a typical particle configuration and (right) the corresponding reconstructed surface mesh; the particle diameter is about 10 nm.
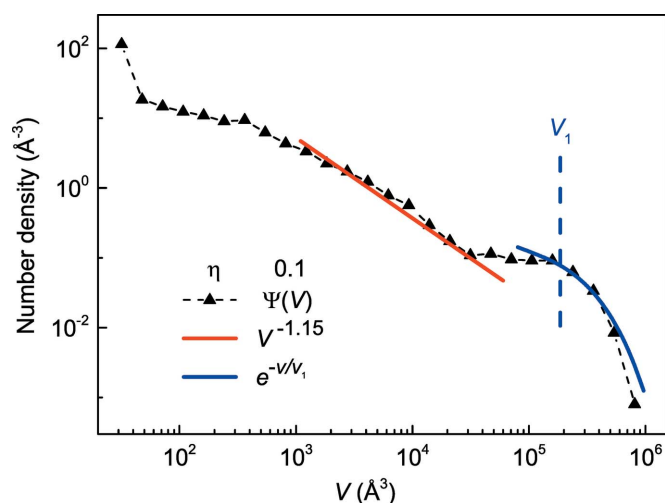
Figure 4
Particle-size distribution upon full fragmentation (440 ps) obtained via cluster analysis for an expansion rate of $\eta = 0.1$ ps^{-1}. The particle-size number distribution can be well described by a power law with an exponent of -1.15 and an exponential function with a characteristic size V_c.

Figure 5
The 2D SAXS pattern of the liquid sheet upon full fragmentation (440 ps, see also Fig. 2) after adiabatic expansion at a rate of $\eta = 0.1$ ps^{-1}.

was proposed by Durand & Soulard (2013). The exponential law describes larger particles from the 1D Poisson fragmentation process of the filaments. The characteristic size for the exponential law is $V_c = 1.85 \times 10^5$ Å^3 as obtained from the fit, and the corresponding radius is $R_c = 35.3$ Å, for an expansion rate of $\eta = 0.1$ ps^{-1}. The transition point between the power law and the exponential law can be readily identified at $V \simeq 5 \times 10^4$ Å^3 ($R \simeq 23$ Å) in Fig. 4.

In the following discussions, exponential and power laws all refer to the number distribution of particle sizes as a function of particle volume, $\Psi(V)$.

4. Resolving nanoscale fragmentation with SAXS

At full fragmentation, particle size distributions, including number size distributions and volume size distributions, are derived via cluster and SAXS analyses, and compared. Two SAXS data-analysis methods, the regularization method for polydisperse systems (Ilavsky & Jemian, 2009) and a modified Guinier method (originally for monodisperse systems; Beaucage *et al.*, 2004), are utilized. Characteristic size and degree of dispersity are extracted from volume size distributions. The effect of expansion rate on size distribution at full fragmentation is also explored.

4.1. SAXS analysis

The 2D SAXS pattern for the liquid sheet upon full fragmentation after adiabatic expansion at an expansion rate of $\eta = 0.1$ ps^{-1} is calculated (Fig. 5) and then integrated azimuthally to obtain the 1D scattering curve (Fig. 6). The regularization method as implemented in the experimental SAXS data-analysis package *Irena* (Ilavsky & Jemian, 2009) is used for retrieving the size distribution. Instead of directly obtaining number size distributions as a function of particle volume,
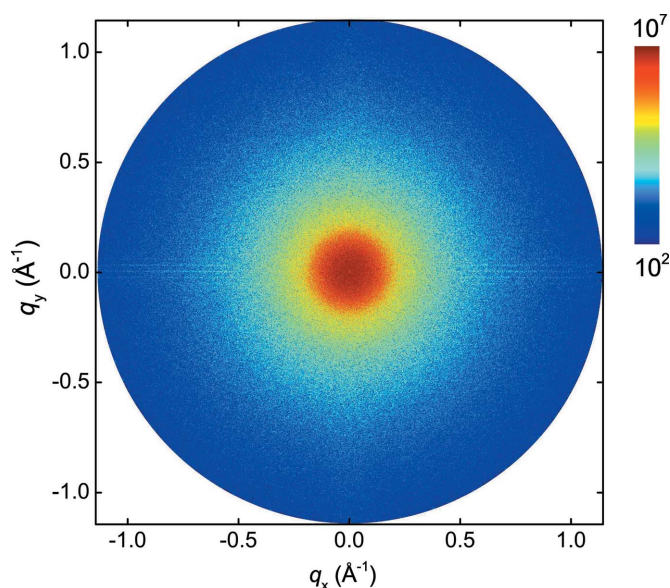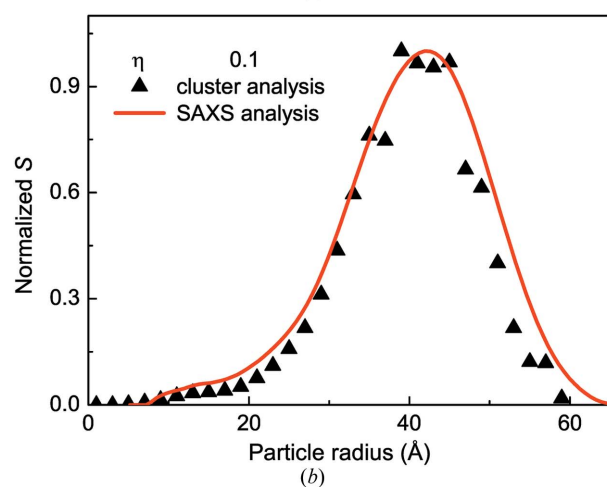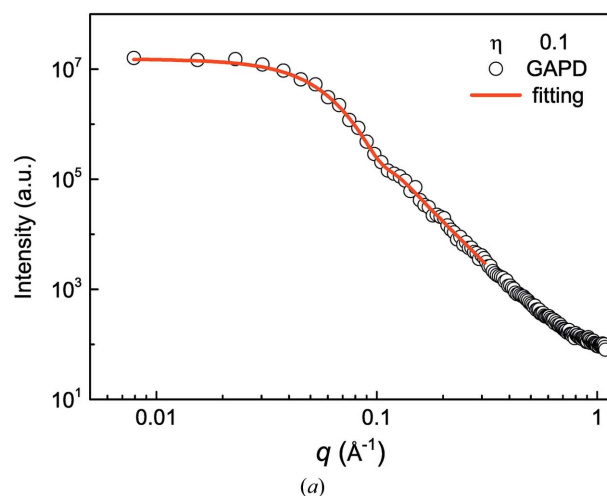

(a)

(b)

Figure 6
(a) The 1D scattering curve and (b) $S(R)$ curves obtained with the regularization method from the scattering curve and cluster analysis. $\eta = 0.1$ ps^{-1}.

$\Psi(V)$, we obtain the particle-volume size distribution, S, as a function of particle radius R from the SAXS analysis with *Irena*. In the following discussions, all $S(R)$ values are normalized to [0, 1].

4.1.1. Particle-volume size distributions. Given $\Psi(V)$ from the cluster analysis, we have

$$\Psi(R) = \Psi[V(R)]\frac{\partial V(R)}{\partial R}. \quad (10)$$

Since $S(R) = \Psi(R)V(R)$, we can convert $\Psi(V)$ obtained from the cluster analysis to $S(R)$ and compare it with the $S(R)$ curve derived from the 1D SAXS curve via the regularization method. The comparison yields excellent agreement in $S(R)$ between the values from the cluster analysis [filled triangles, Fig. 6(b)] and from the SAXS pattern [red curve, Fig. 6(b)]. The main peak and the small shoulder on the left correspond to the exponential and power-law distributions, respectively. The small shoulder in Fig. 6(b) (from the SAXS analysis) appears at $R < 25$ Å, in good accordance with the cluster analysis (< 23 Å).

The $S(R)$ curves derived from SAXS and those from direct cluster analysis are in good agreement overall. However, the particles following the power-law distribution possess a minor volume or mass fraction, so their signature can hardly be identified in $S(R)$ curves [Fig. 6(b)], despite their large number. Hence, it is the larger particles that follow the exponential distribution and dominate the smaller particles following the power law in volume fraction. In the following discussions we will focus on such larger particles following an exponential distribution.

4.1.2. Characteristic sizes and degree of dispersity obtained from $S(R)$. $S(R)$ offers a piece of information of particular interest, characteristic sizes for certain distributions. For the instance of an exponential distribution, $\Psi(V) = A\exp(-V/V_c)$ and $V(R) = \frac{4}{3}\pi R^3$. Then,

$$S(R) = \frac{16}{3}A\pi^2 R^5 \exp\left(-\frac{R^3}{R_c^3}\right). \quad (11)$$

The maximum of $S(R)$ is located at $R_{\max}$, *i.e.*

$$\left.\frac{\partial S(R)}{\partial R}\right|_{R_{\max}} = 0, \quad (12)$$

and it follows that

$$R_{\max} = \left(\frac{5}{3}\right)^{1/3} R_c \simeq 1.186 R_c. \quad (13)$$

This means that one can deduce the characteristic particle size from the location of the maximum of $S(R)$ obtained by SAXS analysis for an exponential size distribution, via equation (13). From Fig. 6, $R_{\max} = 42.6$ Å, so $R_c = 35.9$ Å; this value agrees with R_c from the direct cluster analysis within 1.4%.

The full width at half-maximum (FWHM) of $S(R)$ for an exponential distribution $\Psi(V)$ can also be determined via

$$\frac{S(R)}{S(R_{\max})} = 0.5. \quad (14)$$

Two positive solutions to the above equation are $R = 0.699R_{\max}$ and $1.302R_{\max}$, so $\text{FWHM}_S = 0.603R_{\max}$. We introduce the polydispersity, P, for an exponential size number distribution, defined as

$$P_S = \frac{\text{FWHM}_S}{R_{\max}}. \quad (15)$$

Thus, the ideal value of P_S is 60.3% for exponential size distributions, regardless of the characteristic size. From the SAXS and cluster analyses, we obtain P_S from the particle-size distributions at full fragmentation ($\eta = 0.1$ ps^{-1}) as 49.4 and 42.3%, respectively. The deviations are likely to be caused by the small sampling size in our simulations, but are still acceptable.

4.1.3. Deducing characteristic sizes with the modified Guinier approach. The widely used Guinier approach, originally intended for monodisperse systems, can also be used to derive characteristic sizes for polydisperse systems after certain modification (the modified Guinier approach). For a monodisperse system, the radius of gyration, R_g, of primary particles can be obtained under the Guinier approximation as

$$I(q) = I(0)\exp\left(-\frac{1}{3}q^2 R_g^2\right), \quad (16)$$

for $qR_g < 1.3$ (Feigin & Svergun, 1987). The particle radius R follows as $R = (5/3)^{1/2}R_g$ for monodisperse spherical particles.

Given the simplicity of the Guinier approach, it is desirable to extend its use to polydisperse systems with sizes spanning a few orders of magnitude. In the modified Guinier approach, the 'average' particle size for a polydisperse system is the square root of the volume-squared-weighted mean radius (Beaucage *et al.*, 2004)

$$R_{\text{weighted}} = \left(\frac{\int V(R)^2 \Psi(R)R^2\,dR}{\int V(R)^2 \Psi(R)\,dR}\right)^{1/2}. \quad (17)$$

Presumably, the measured radius of gyration for a polydisperse system is also volume-squared weighted and similar to a monodisperse system, $R_{\text{weighted}} = (5/3)^{1/2}R_{g,\text{weighted}}$. For a polydisperse system with an exponential size number distribution, $\Psi(V) = A\exp(-V/V_c)$. We have from equation (10)

$$R_{\text{weighted}} = R_c\left[\frac{\int t^{10}\exp(-t^3)\,dt}{\int t^8\exp(-t^3)\,dt}\right]^{1/2}, \quad (18)$$

where $t = R/R_c$. In principle, the integration in equation (18) should be conducted from zero to infinity, and we have $R_{\text{weighted}} \simeq 1.44R_c$ for polydisperse systems with exponential size number distributions, independent of particle size. However, in our case, the radius is effectively below $1.66R_c$ [Fig. 7(b)], and $R_{\text{weighted}} \simeq 1.32R_c$.

Volume-squared-weighted radii of gyration for different strain rates are obtained by fitting the low-q portions of the scattering curves (Fig. 8) and the corresponding characteristic sizes are deduced (Table 1). The absolute relative errors for the modified Guinier method are less than 3%, comparable with those for the regularization method. However, the high accuracy of this method relies on *a priori* knowledge of the
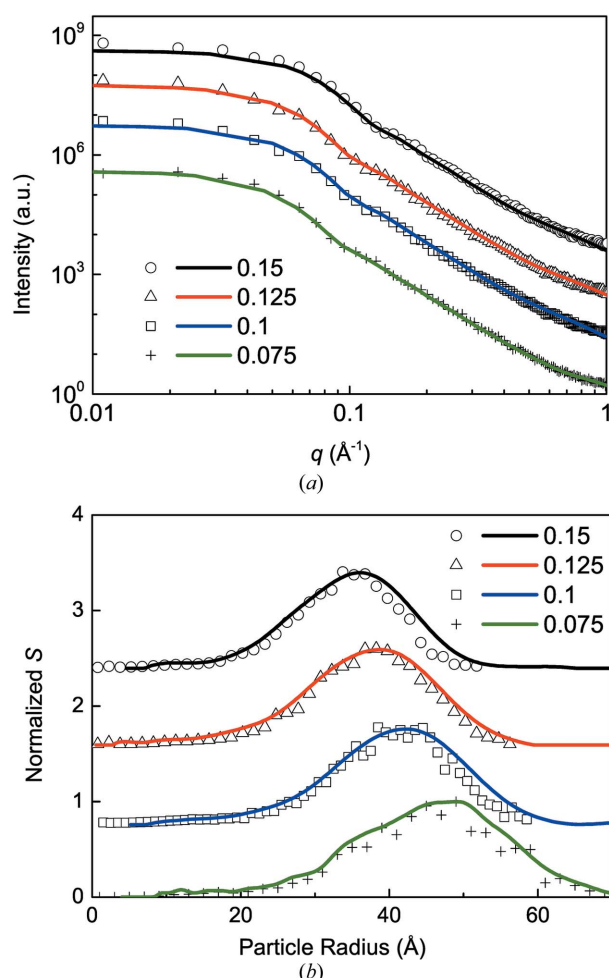
Figure 7
(a) 1D scattering curves obtained by integrating simulated 2D patterns (open symbols) and the fitting results with the regularization method (solid lines). (b) The corresponding $S(R)$ curves for different expansion rates obtained by analyzing the 1D scattering curves with the regularization method (solid lines) and by analyzing the atomic configurations using the cluster analysis method (open symbols). Numbers denote η (ps^{-1}).

particle size distributions, while such prior information is not required for the regularization method.

4.2. Effect of expansion rate

MD simulations of uniaxial adiabatic expansion of liquid sheets are performed at different expansion rates, $\eta = 0.075$, 0.1, 0.125 and 0.15 ps^{-1}, and 2D and 1D scattering patterns are calculated [Fig. 7(a)]. Particle-volume size distributions and average sizes at full fragmentation are obtained from SAXS patterns via the regularization method and the modified Guinier method, and compared with those obtained directly via cluster analysis. A relation between characteristic particle size and expansion rate is obtained.

At full fragmentation, the $S(R)$ curves for different strain rates obtained via cluster analysis [symbols, Fig. 7(b)] and SAXS analysis with the regularization method [lines, Fig. 7(b)] are in excellent accord. (The same fitting parameters are used

Table 1
Characteristic sizes (R_c) for liquid fragmentation with different strain rates obtained by different methods.

Error here refers to the error relative to R_c obtained from cluster analysis.

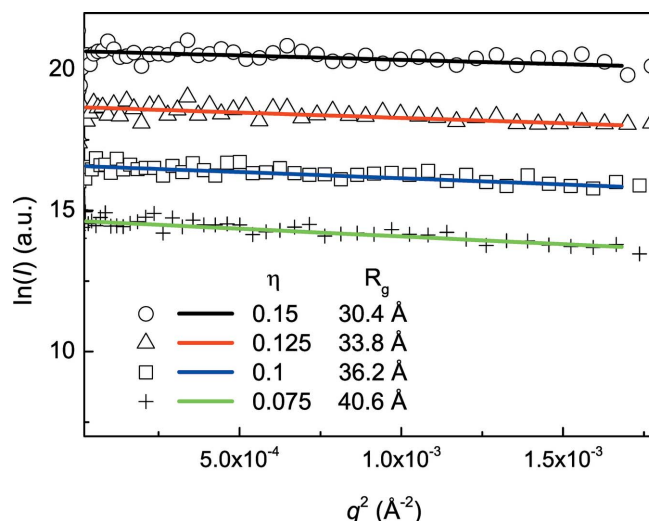|	Cluster analysis	$S(R)$		Guinier method	
η (ps^{-1})	R_c (Å)	R_c (Å)	Error (%)	R_c (Å)	Error (%)
0.150	30.1	30.4	1.0	29.7	−1.3
0.125	32.3	32.3	0.0	33.1	−2.5
0.100	35.4	35.9	1.4	35.4	0.0
0.075	39.8	41.3	3.8	39.7	−0.5

Figure 8
Guinier plots for different strain rates obtained via the weighted Guinier analysis. Fitting is performed within $0.005 < qR_g < 1.6$. The systematic error of this fit is less than 10% for homogeneous spheres.

to retrieve the size distribution from SAXS patterns.) Higher expansion rates lead to smaller particle sizes [Fig. 7(b)]. The corresponding characteristic sizes obtained from the $S(R)$ curves are also in good agreement with those obtained from cluster analysis (within 4%; Table 1).

$R_c(\eta)$ is obtained with the regularization [$S(R)$] method, the weighted Guinier method and the cluster analysis. As shown in Table 1, the characteristic particle size, R_c, is strongly dependent on the strain rate, and higher strain rates lead to smaller particle sizes. The results agree with each other and all show linear relations in the log–log plots (Fig. 9); their slopes (exponents) are -0.45 ± 0.02, -0.40 ± 0.03 and -0.40 ± 0.03. Hence, the relation between the characteristic size R_c and the strain rate η can be described by a rate-dependent power law.

5. Implications for experiments on XFELs

XFEL pulse widths vary in the range of 10–100 fs, and we consider below the effect of XFEL pulse width on SAXS patterns and size distribution determination for the full range of 0–100 fs. Anisotropic SAXS patterns for the second stage of fragmentation (disintegration of networks) are examined as a forward simulation example of more complicated processes to aid data interpretation. Possible implementation of the
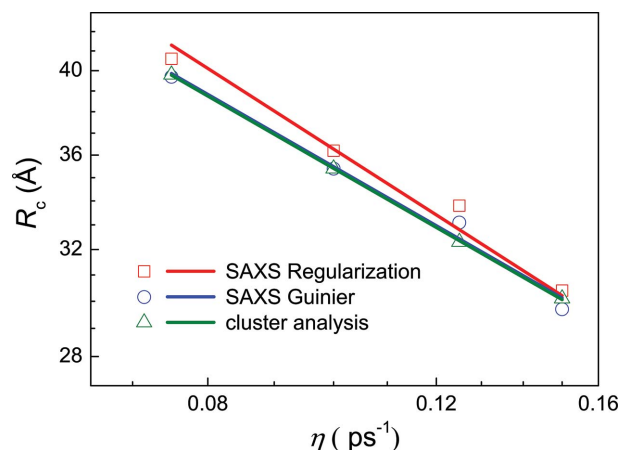
Figure 9
A log–log plot of the characteristic size R_c as a function of expansion rate η. Solid lines denote linear fits.

proposed measurements at an XFEL source is discussed as well.

5.1. Effect of pulse width

To evaluate the effect of X-ray pulse width, scattering patterns for an expansion rate of $\eta = 0.1$ ps^{-1} with pulse durations of 0 (snapshot), 10, 50 and 100 fs are calculated. Here, $\tilde{I}(\mathbf{q})$ is obtained by discretizing equation (6), *i.e.* super-imposing the individual scattering signals $I(\mathbf{q}, t)$ which are equally distributed in $[t, t + \tau]$, and $\Delta t = 2$ fs.

For stage 3, fragmentation largely stops while the total system volume continues to expand. The configurations are still dynamic and evolving. We take configurations within the pulse width centered at $t = 440$ ps and calculate the corresponding SAXS patterns. The resultant 1D scattering curves are smoother for pulse durations of 10, 50 and 100 fs than for the snapshot due to better statistics [Fig. 10(a)], indicating a better signal-to-noise ratio in real experiments due to a longer acquisition time. Fig. 10(b) demonstrates that no obvious deviations of the resultant $S(R)$ curves (analyzed with the regularization method) are observed for pulse durations of 10, 50 and 100 fs. The slight deviation of the $S(R)$ curves for finite pulse widths from that for the snapshot and others at the small/large size limits arises from the better smoothness of the scattering curves for longer pulse durations. For more complicated cases as in stage 2 (see below), varying the pulse width between 0 and 100 fs also has a negligible effect on the SAXS patterns and subsequent analysis.

5.2. Early stages of fragmentation

Early stages such as stage 2 (the disintegration of cellular structures) are also of interest. However, the configuration is highly anisotropic [Fig. 11(a), filaments tend to lie in the direction of expansion] and different subcells are connected or close to each other (*i.e.* the assumption of a dilute system is not valid anymore). *GAPD* makes it possible for us to simulate fully coherent scattering patterns for such systems with strong anisotropy and interparticle interaction (E *et al.*, 2018).


(a)

(b)
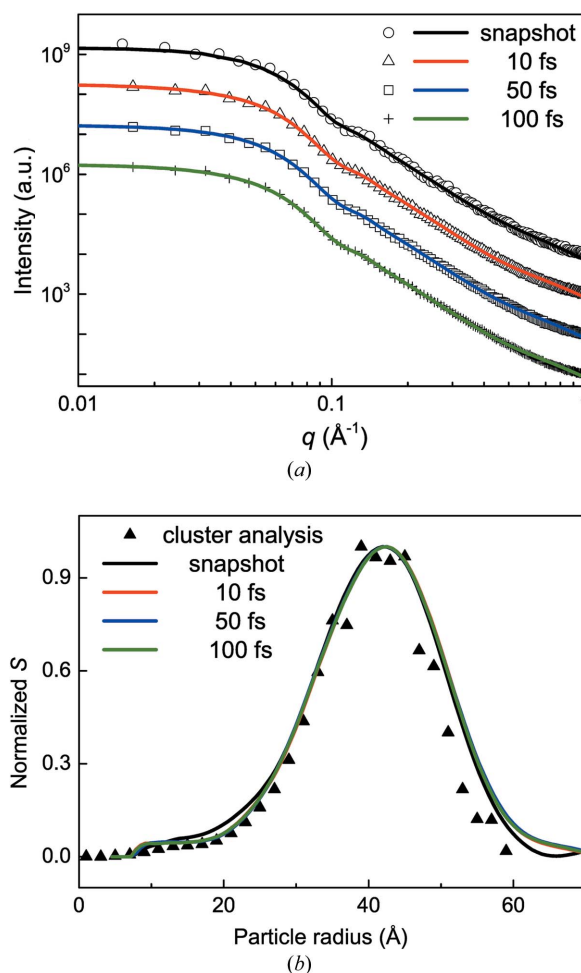
Figure 10
The effect of pulse width on the determination of particle-size distribution at the full fragmentation stage ($t = 440$ ps, stage 3). Expansion rate $\eta = 0.1$ ps^{-1}. (a) 1D scattering curves obtained for different pulse durations. Solid lines denote intensity fits. (b) The corresponding $S(R)$ for different pulse durations.

2D scattering patterns during stage 2 near $t = 80$ ps are calculated for X-ray pulse durations of 0 (snapshot), 10, 50 and 100 fs. An anisotropic intensity distribution can be clearly observed in the 2D scattering patterns [Fig. 11(b)], indicating the existence of anisotropic structures, which is in accord with the MD configurations (disintegration of cellular structures). As an example, two segments (vertical and horizontal, or V and H) of the 2D patterns are azimuthally integrated within 30°. Direct simulations with such programs as *GAPD* are necessary for data interpretation of such anisotropic 2D scattering patterns.

For XFEL pulse durations up to 100 fs, the differences in the SAXS patterns are negligible [Fig. 11(c)]. Hence, SAXS measurements with pulse durations up to 100 fs are feasible to probe such fragmentation dynamics at stages 2 and 3. With regard to stage 1 (predominantly void nucleation and growth), it can also be probed by ultrafast SAXS measurements. However, the process differs significantly from fragmentation (stages 2 and 3) and is beyond the scope of this work.
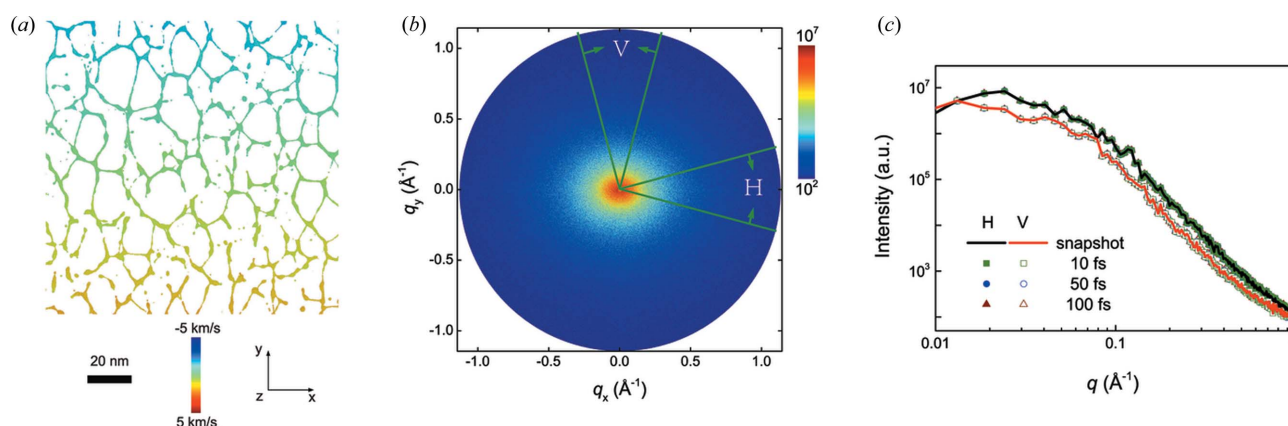
Figure 11
Anisotropic SAXS patterns at stage 2 (disintegration of cells). (*a*) An MD snapshot of the real-space structure at t = 80 ps. (*b*) The corresponding anisotropic 2D SAXS pattern. Vertical (V) and horizontal (H) segments (30° wide) along the azimuthal direction are analyzed independently. (*c*) 1D scattering curves of the selected segments for different pulse widths.

5.3. Statistics of obtained data

As constrained by computational capability, the X-ray beam size and system size are limited to approximately 1.5 µm × 4.0 µm. For real XFEL experiments, the beam size ranges from 10 to 100 µm (order of magnitude). With a beam size of 100 µm × 100 µm, the illuminated area is about 1.7×10^3 times larger than that used in this work. Therefore, much better data statistics are expected in real XFEL experiments.

5.4. Potential XFEL experiments

5.4.1. Generation of liquid sheets.
Liquid sheets can be produced from shocked metallic foils (tens to hundreds of micrometres thick) with surface grooves (*e.g.* sinusoidal grooves). Intense shock loading delivered by high-power laser irradiation drives the growth of the Richtmyer–Meshkov instability (Brouillette, 2002) from a grooved surface into metallic jets. Melting on shock or release of the jets forms liquid sheets. The dynamic event durations are normally below 1 ns. Various effects on the size distribution of nanoparticles at full fragmentation, such as the scaled perturbation amplitude for a sinusoidal surface (De Rességuier *et al.*, 2016), half-angle and groove size and shock breakout pressure, can be investigated. On the other hand, high-pressure liquid jets forced through a shaped nozzle can also be used to produce liquid jets.

5.4.2. Ultrafast SAXS measurements.
X-rays are incident along the plane normal of a liquid sheet (Fig. 1). As shown above, the pulse width of current XFEL sources (10–100 fs) such as the European XFEL and LCLS is sufficiently narrow for SAXS measurements on ultrafast dynamic events. Probing the XFEL pulse for single-pulse SAXS measurements is synchronized with a high-power laser, and a certain delay is introduced between the laser loading and the X-ray probe to obtain snapshots at different stages of fragmentation. Direct X-ray detectors with low noise like AGIPD at the European XFEL are preferred for data acquisition.

6. Conclusions

We have investigated the feasibility of resolving the nanoscale fragmentation of liquids with ultrafast SAXS via large-scale MD simulations. A relation between particle-volume size distribution and particle-number size distribution has been determined. SAXS data interpretation, including the retrieval of particle-volume size distribution via the regularization method and average size determination with the weighted Guinier method, has been explored. The particle sizes obtained from simulated SAXS are in excellent agreement with results from direct cluster analysis. The effect of expansion rate on the final particle size distributions and characteristic sizes have been explored. Our results show that, for XFEL pulses up to ~100 fs, the effect of pulse width on SAXS measurements of ultrafast fragmentation of liquids can be neglected. For a liquid sheet dynamically loaded to full fragmentation, the particle size distribution can be described with a combination of a power law and an exponential function, and the rate dependence of the characteristic size with a rate-dependent power law. Data interpretation for earlier fragmentation stages with anisotropic scattering patterns requires forward SAXS simulations. Our results demonstrate the feasibility of resolving the nanoscale dynamics of fragmentation and similar processes with SAXS, and provide guidance for future XFEL experiments and data interpretation.

research papers

References

An, Q., Luo, S.-N., Han, L.-B., Zheng, L. & Tschauner, O. (2008). *J. Phys. Condens. Matter*, **20**, 095220.

Ashurst, W. T. & Holian, B. L. (1999). *Phys. Rev. E*, **59**, 6742–6752.

Åström, J., Holian, B. & Timonen, J. (2000). *Phys. Rev. Lett.* **84**, 3061–3064.

Beaucage, G., Kammler, H. K. & Pratsinis, S. E. (2004). *J. Appl. Cryst.* **37**, 523–535.

Boast, C. & Baveye, P. (2017). *Revival: Fractals in Soil Science (1998)*, edited by P. Baveye, J.-Y. Parlange and B. A. Stewart, pp. 9–62. Boca Raton: CRC Press.

Bontaz-Carion, J. & Pellegrini, Y.-P. (2006). *Adv. Eng. Mater.* **8**, 480–486.

Bringa, E., Cazamias, J., Erhart, P., Stölken, J., Tanushev, N., Wirth, B., Rudd, R. & Caturla, M. (2004). *J. Appl. Phys.* **96**, 3793–3799.

Brouillette, M. (2002). *Annu. Rev. Fluid Mech.* **34**, 445–468.

Buttler, W., Oró, D., Preston, D., Mikaelian, K., Cherne, F., Hixson, R., Mariam, F., Morris, C., Stone, J., Terrones, G. & Tupa, D. (2012). *J. Fluid Mech.* **703**, 60–84.

Cai, Y., Wu, H. & Luo, S. (2014). *J. Chem. Phys.* **140**, 214317.

Chen, S. & Luo, S.-N. (2018). *J. Synchrotron Rad.* **25**, 496–504.

Durand, O. & Soulard, L. (2012). *J. Appl. Phys.* **111**, 044901.

Durand, O. & Soulard, L. (2013). *J. Appl. Phys.* **114**, 194902.

E, J. C., Wang, L., Chen, S., Zhang, Y. Y. & Luo, S. N. (2018). *J. Synchrotron Rad.* **25**, 604–611.

Edelsbrunner, H. & Mücke, E. P. (1994). *ACM Trans. Graph.* **13**, 43–72.

Feigin, L. & Svergun, D. (1987). *Structure Analysis by Small-Angle X-ray and Neutron Scattering.* New York: Plenum Press.

Fox, A. G., O'Keefe, M. A. & Tabbernor, M. A. (1989). *Acta Cryst.* A**45**, 786–793.

Goncharov, V. (1999). *Phys. Rev. Lett.* **82**, 2091–2094.

Grady, D. (2007). *Fragmentation of Rings and Shells: The Legacy of N. F. Mott.* New York: Springer Science & Business Media.

Grady, D. (2009). *Dynamic Fragmentation of Solids. Shock Wave Science and Technology Reference Library*, Vol. 3, *Solids II*, edited by Y. Horie, pp. 169–276.

Grady, D. E. (2010). *Int. J. Fracture*, **163**, 85–99.

He, A.-M., Wang, P. & Shao, J.-L. (2015). *Chin. Phys. B*, **25**, 017102.

He, A.-M., Wang, P. & Shao, J.-L. (2016). *Modell. Simul. Mater. Sci. Eng.* **24**, 025002.

Holian, B. L. & Grady, D. E. (1988). *Phys. Rev. Lett.* **60**, 1355–1358.

Ilavsky, J. & Jemian, P. R. (2009). *J. Appl. Cryst.* **42**, 347–353.

Kluge, T., Gutt, C., Huang, L., Metzkes, J., Schramm, U., Bussmann, M. & Cowan, T. E. (2014). *Phys. Plasmas*, **21**, 033110.

Li, B., Wang, L. E. J., Ma, H. & Luo, S. (2014). *J. Appl. Phys.* **116**, 213506.

Li, B., Zhao, F., Wu, H. & Luo, S. (2014). *J. Appl. Phys.* **115**, 073504.

Li, X., Wei, Y., Lu, L., Lu, K. & Gao, H. (2010). *Nature*, **464**, 877–880.

Michel, P., Benz, W., Tanga, P. & Richardson, D. C. (2001). *Science*, **294**, 1696–1700.

Mishin, Y., Mehl, M., Papaconstantopoulos, D., Voter, A. & Kress, J. (2001). *Phys. Rev. B*, **63**, 224106.

Monfared, S., Oró, D., Grover, M., Hammerberg, J., LaLone, B., Pack, C., Schauer, M., Stevens, G., Stone, J., Turley, W. & Buttler, W. T. (2014). *J. Appl. Phys.* **116**, 063504.

Monfared, S. K., Buttler, W. T., Frayer, D. K., Grover, M., LaLone, B. M., Stevens, G. D., Stone, J. B., Turley, W. D. & Schauer, M. M. (2015). *J. Appl. Phys.* **117**, 223105.

Morris, C. L., Brown, E. N., Agee, C., Bernert, T., Bourke, M. A. M., Burkett, M., Buttler, W., Byler, D. D., Chen, C.-F., Clarke, A. J., Cooley, J. C., Gibbs, P. J., Imhoff, S. D., Jones, R., Kwiatkowski, K., Mariam, F. G., Merrill, F. E., Murray, M. M., Olinger, C. T., Oro, D. M., Nedrow, P., Saunders, A., Terrones, G., Trouw, F., Tupa, D., Vogan, W., Winkler, B., Wang, Z. & Zellner, M. B. (2016). *Exp. Mech.* **56**, 111–120.

Plimpton, S. (1995). *J. Comput. Phys.* **117**, 1–19.

Rességuier, T. de, Roland, C., Prudhomme, G., Lescoute, E., Loison, D. & Mercier, P. (2016). *J. Appl. Phys.* **119**, 185108.

Sorenson, D., Capelle, G., Grover, M., Johnson, R., Kaufman, M., LaLone, B., Malone, R., Marshall, B., Minich, R., Pazuchanics, P., Smalley, D. D., Stevens, G. D., Tunnell, T. W. & Turley, W. D. (2017). *J. Dyn. Behav. Mater.* **3**, 233–239.

Sorenson, D. S., Pazuchanics, P., Johnson, R. P., Malone, R. M., Kaufman, M. I., Tunnell, T. W., Tibbitts, A., Capelle, G. A., Grover, M., Marshall, B., Stevens, G. D., LaLone, G., Turley, D. & Marks, D. (2014). *Ejecta Particle Formation from Micro-Jets (U)*. Technical Report LA-UR-14-23036. Los Alamos National Laboratory, New Mexico, USA.

Stukowski, A. (2014). *JOM*, **66**, 399–407.

Thomas, V. A. & Kares, R. J. (2012). *Phys. Rev. Lett.* **109**, 075004.

Wadell, H. (1935). *J. Geol.* **43**, 250–280.

Wagner, N. J., Holian, B. L. & Voter, A. F. (1992). *Phys. Rev. A*, **45**, 8457–8470.

Warren, B. E. (1969). *X-ray Diffraction.* New York: Dover Publications Inc.